

New Mechanism for Ferroelectricity in the Perovskite $\text{Ca}_{2-x}\text{Mn}_x\text{Ti}_2\text{O}_6$ Synthesized by Spark Plasma Sintering

Zongyao Li,[†] Yujin Cho,[‡] Xiang Li,[†] Xinyu Li,[†] Akihisa Aimi,[§] Yoshiyuki Inaguma,^{||} Jose A. Alonso,[⊥] Maria T. Fernandez-Diaz,[#] Jiaqiang Yan,[∇] Michael C. Downer,[‡] Graeme Henkelman,[¶] John B. Goodenough,[†] and Jianshi Zhou^{*,†}

[†]Material Science and Engineering Program, Mechanical Engineering, University of Texas at Austin, Austin, Texas 78712, United States

[‡]Department of Physics, University of Texas at Austin, Austin, Texas 78712, United States

[§]Department of Pure and Applied Chemistry, Faculty of Science and Technology, Tokyo University of Science, 2641 Yamazaki, Noda-shi, Chiba 278-8510, Japan

^{||}Department of Chemistry, Faculty of Science, Gakushuin University, 1-5-1 Mejiro, Toshima-ku, Tokyo 171-8588, Japan

[⊥]Instituto de Ciencia de Materiales de Madrid, CSIC, Cantoblanco, E-28094 Madrid, Spain

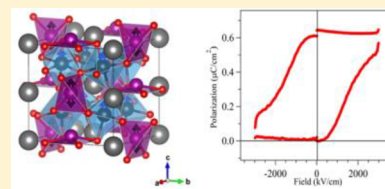
[#]Institut Laue-Langevin (ILL), 156X, F-38042 Grenoble Cedex 9, France

[∇]Materials Science and Technology Division, Oak Ridge National Laboratory, Oak Ridge, Tennessee 37831, United States

[¶]Department of Chemistry, University of Texas at Austin, Austin, Texas 78712, United States

Supporting Information

ABSTRACT: Perovskite oxides hosting ferroelectricity are particularly important materials for modern technologies. The ferroelectric transition in the well-known oxides BaTiO_3 and PbTiO_3 is realized by softening of a vibration mode in the cubic perovskite structure. For most perovskite oxides, octahedral-site tilting systems are developed to accommodate the bonding mismatch due to a geometric tolerance factor $t = (A-O)/[\sqrt{2}(B-O)] < 1$. In the absence of cations having lone-pair electrons, e.g., Bi^{3+} and Pb^{2+} , all simple and complex A-site and B-site ordered perovskite oxides with a $t < 1$ show a variety of tilting systems, and none of them become ferroelectric. The ferroelectric $\text{CaMnTi}_2\text{O}_6$ oxide is, up to now, the only one that breaks this rule. It exhibits a columnar A-site ordering with a pronounced octahedral-site tilting and yet becomes ferroelectric at $T_c \approx 650$ K. Most importantly, the ferroelectricity at $T < T_c$ is caused by an order–disorder transition instead of a displacive transition; this character may be useful to overcome the critical thickness problem experienced in all proper ferroelectrics. Application of this new ferroelectric material can greatly simplify the structure of microelectronic devices. However, $\text{CaMnTi}_2\text{O}_6$ is a high-pressure phase obtained at 7 GPa and 1200 °C, which limits its application. Here we report a new method to synthesize a gram-level sample of ferroelectric $\text{Ca}_{2-x}\text{Mn}_x\text{Ti}_2\text{O}_6$, having the same crystal structure as $\text{CaMnTi}_2\text{O}_6$ and a similarly high Curie temperature. The new finding paves the way for the mass production of this important ferroelectric oxide. We have used neutron powder diffraction to identify the origin of the peculiar ferroelectric transition in this double perovskite and to reveal the interplay between magnetic ordering and the ferroelectric displacement at low temperatures.



1. INTRODUCTION

The cubic ABO_3 perovskite structure consists of corner-shared BO_6 octahedra with B atoms at the corner and A atoms in the body center of the unit cell. A tolerance factor $t = (A-O)/[\sqrt{2}(B-O)]$ is a measure of the mismatch between the equilibrium A–O and B–O bond lengths. A $t < 1$ is accommodated by a cooperative rotation of the BO_6 octahedra that lowers the crystal symmetry;¹ a $t > 1$ is accommodated by the formation of a hexagonal polytype or by a ferroelectric (or antiferroelectric) displacement that creates asymmetric B–O and/or A–O bonds if B is a d^0 transition-metal cation, and/or A has an s^2 core of lone-pair electrons, e.g., Bi(III) or Pb(II) .² The relationship between the t -factor and ferroelectricity is well-illustrated by the ATiO_3 family in which A = Ca has $t < 1$,

A = Sr has $t \approx 1$, and A = Ba has a $t > 1$ at room temperature. BaTiO_3 undergoes ferroelectric distortions. SrTiO_3 normally exhibits a cooperative rotation of the TiO_6 octahedra at low temperature, but substitution of ^{18}O for ^{16}O can trigger a low-temperature ferroelectric distortion.^{3–5} Ferroelectric antisymmetric cation–anion bonds have not been found in perovskite oxides without the s^2 core A-site cations where the BO_6 octahedra undergo cooperative rotations.^{6,7}

Benedek and Fennie⁷ have performed very interesting computer experiments. The frequency of the ferroelectric mode has been calculated as a function of the t -factor for

Received: October 27, 2017

Published: January 15, 2018

perovskite oxides with the cubic $Pm\bar{3}m$ and the orthorhombic $Pbnm$ symmetries. Their results show that the ferroelectric transition is essentially suppressed in the $Pbnm$ perovskites, independent of the tilting magnitude. The $a^-a^-c^+$ tilting system of the $Pbnm$ structure can be decomposed into two sub systems labeled $a^-a^-c^0$ and $a^0a^0c^+$, which allows illustrating the rotation-wise ferroelectric instability. Whereas ferroelectricity is more easily obtained in the cubic phase than in the subgroups of $a^-a^-c^0$ and $a^0a^0c^+$, a ferroelectric instability becomes achievable in the phase with the $a^0a^0c^+$ tilting system as the octahedral tilting along the c axis increases. It is the A-site displacement associated with the $a^-a^-c^0$ tilting mode that suppresses the ferroelectric mode strongly. The A-site antipolar displacements and associated tilting can be suppressed in a heterogeneous structure, such as an $\text{La}_2\text{NiMnO}_6$ film on a SrTiO_3 substrate⁸ and in a NdNiO_3 film on a LaAlO_3 substrate⁹ where ferroelectricity has indeed been found.

Double perovskites with a more general formula $\text{AA}'\text{BB}'\text{O}_6$ can show even more complicated tilting systems and A-site environments.^{10–12} Cations at both the A site and B site can be ordered into a rock-salt, columnar, or layered structure.¹¹ Among these double perovskites, few of them adopt a polar structure like NaRMnWO_6 ($R = \text{La, Nd, Tb}$) with a $P2_1$ phase caused by layered ordering of A-site cations and rock-salt ordering of the B-site cations, which has the $a^-a^-c^+$ tilting system.¹³ Density functional theory (DFT) calculations have predicted that double perovskites with this structure are ferroelectric.¹⁴ However, switchable ferroelectricity was not found experimentally for any of these three double perovskites.¹⁵

$\text{CaMnTi}_2\text{O}_6$ is the only switchable ferroelectric double perovskite that is Pb^{2+} or Bi^{3+} free.¹⁶ The columnar ordering of A-site cations found in $\text{CaFeTi}_2\text{O}_6$ is a rare case.¹⁷ The octahedral-site tilting in the tilt system $a^+a^+c^-$ ($P4_2/nmc$) places Ca^{2+} in columns along the c -axis; every Ca column is surrounded by Fe columns consisting of alternating FeO_4 tetrahedra and coplanar FeO_4 . Although the space group allows Fe^{2+} to be displaced off the plane of the coplanar FeO_4 units, Fe^{2+} stays perfectly in the plane formed by four oxygen; this compound is not ferroelectric as determined by a measurement of second harmonic generation at room temperature. The double perovskite $\text{CaMnTi}_2\text{O}_6$ adopts the same crystal structure as $\text{CaFeTi}_2\text{O}_6$ at high temperatures.¹⁶ The only difference is that the Mn^{2+} is displaced off the MnO_4 plane, which is allowed by symmetry, but it is randomly displaced along the c -axis above T_c , shown in Figure 1(a). At $T < T_c$, however, all the displacements of Mn^{2+} at the coplanar sites are in the same direction along the c -axis. Correspondingly, Mn cations in tetrahedra and Ti in octahedra are polarized, as shown in Figure 1(b). The polarization is switchable under an external electric field. Since the nonpolar $\text{CaFeTi}_2\text{O}_6$ is in the identical tilting system, ferroelectricity in $\text{CaMnTi}_2\text{O}_6$ is clearly driven by manganese, most likely by the Mn ions in the coplanar coordination. The disorder–order type of ferroelectric transition is rare and offers a fundamentally different mechanism from the well-discussed cases of proper, improper, hybrid improper ferroelectricity¹⁸ and may find potentially new applications. Gaining a fundamental understanding of the mechanism triggering the ferroelectric transition is critically important for applications of the new ferroelectric oxide and for designing new ferroelectric materials. To this end, a thorough structural study by neutron diffraction is needed. Moreover, since the ferroelectric $\text{CaMnTi}_2\text{O}_6$ is a high pressure phase, it is

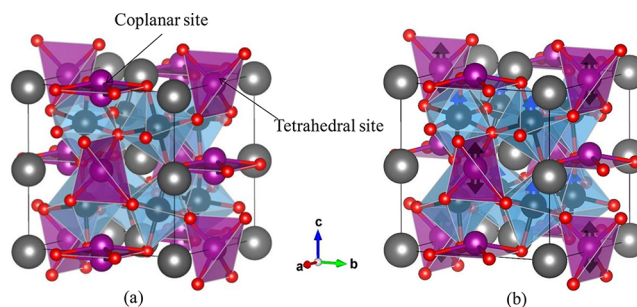


Figure 1. Structural models of (a) nonpolar and (b) polar $\text{CaMnTi}_2\text{O}_6$. Like the simple perovskite, the framework of double perovskite structure consists of corner-shared TiO_6 octahedra. The columnar ordering means that the A-site Ca are ordered in columns along the c axis, which are surrounded by the Mn columns. The space group of the nonpolar double perovskite allows that Mn^{2+} at the coplanar sites shift out of the plane and the shifting direction is random between the Mn sites. The polar double perovskite structure is different from the nonpolar one by (i) all Mn^{2+} at coplanar sites are ordered with the same shifting direction along the c axis, as can be observed in the structural mode (b); (ii) Ti^{4+} cations shift from the center of the octahedral sites and the Ti–O bond length splitting is enhanced dramatically; (iii) Mn^{2+} cations at tetrahedral-sites also shift from center of the tetrahedra, but the shifting direction is temperature dependent. Arrows in (b) indicate the direction of atomic displacement.

necessary to explore an alternative approach to synthesize the material in larger quantities.

2. EXPERIMENTAL SECTION

Synthesis. A mixture of $x\text{MnO}$, $x\text{TiO}_2$ and $(2-x)\text{CaTiO}_3$ was used as the starting materials. The sintering was performed with a SPS system model 10–3 from Thermal Technology LLC at 1350 °C under 90 MPa for 1 min within a 20 mm diameter graphite die.

Structural Characterization. The obtained pellets with orange color were crushed into powders for the characterization by X-ray diffraction. Rigaku Miniflex 600 with $\text{Cu K}\alpha$ radiation was used to determine the phase purity. Neutron powder diffraction experiments were performed in the temperature range of 1.5 to 540 K with wavelength 2.52 Å and from 393 to 703 K with wavelength 1.59 Å at Institut Laue-Langevin (ILL), France. Neutron powder diffraction measurements on a different batch of the SPS sample were performed with POWGEN located at the Spallation Neutron Source (SNS) at Oak Ridge National Laboratory. All diffraction patterns are refined by the Rietveld method with the FullProf software.¹⁹ The actual Mn concentration x in the SPS products was determined by measuring the temperature dependence of paramagnetic susceptibility with a Physical Property Measurement System (PPMS) (Quantum Design).

Ferroelectric Characterization. A well-polished bulk sample was used to measure the temperature dependence of the optical Second Harmonic Generation (SHG). Ti:sapphire laser at 780 nm wavelength (76 MHz repetition rate, 150 fs pulse width) was incident on the sample at 45°. A photomultiplier tube (PMT) detected 390 nm s-polarized SHG generated by s-polarized incoming light that is insensitive to the surface, but is sensitive to centrosymmetry-breaking in a crystal structure caused by a ferroelectric transition. For dielectric property measurements, the polycrystalline sample was polished to a thickness of 0.29 mm for permittivity and 0.18 mm for the P – E hysteresis loop; Au electrodes were deposited on both sides of the pellet by a dc sputtering method. Dielectric permittivity measurements were performed with an Agilent 4284 precision LCR meter for frequencies of 1 kHz to 1 MHz. The ferroelectric property was evaluated by a P – E hysteresis loop measurement at 200 Hz with an aixACCT Easy Check and TF Analyzer 2000 ferroelectric tester at room temperature.

DFT Calculation. Spin polarized DFT calculations were performed with the projector augmented wave method,^{20,21} as implemented in the Vienna Ab Initio simulation package.^{22–24} Electron exchange and correlation was described within the generalized gradient approximation by using the Perdew–Burke–Ernzerh functional. A Hubbard term was added to the d orbitals of Mn and Ti with an effective U value of 3.8 and 4.36 eV, respectively. A $5 \times 5 \times 5$ k-point mesh, a plane wave cutoff of 600 eV, and a force convergence tolerance of 2.5 meV/Å were employed for structural relaxation. Phonon frequencies were calculated with density functional perturbation theory.

3. RESULTS AND DISCUSSION

Double Perovskites and Spark Plasma Sintering (SPS).

For the double perovskites $AA'B'B'O_6$ or the A-site ordered perovskites $AA'_3B_2B''_2O_{12}$, whether the perovskite phase is stable depends on the global instability index (GII) in addition to the t factor; GII is defined as the difference between the bond valence sum (BVS) and the formal valence of cations and anions in a complex oxide. A survey in the literature on this issue indicates that high-pressure synthesis is normally required if GII is larger than 0.02 for a given complex oxide formula.^{25–30} A calculation using the software SPuDS gives a $GII = 0.219$ for $CaMnTi_2O_6$, which is why high-pressure synthesis is required to stabilize this double perovskite. However, high-pressure synthesis is not the only way to obtain a complex oxide with a high GII. For example, an A-site ordered perovskite $CaCu_3Fe_2Sb_2O_{12}$ with a $GII = 0.033$, which has been obtained previously with high-pressure synthesis,²⁹ can be synthesized at ambient pressure through a designed chemical procedure.³¹ The same procedure, however, did not work to synthesize the double perovskite $CaMnTi_2O_6$. The issue for us to consider is whether the SPS synthesis could help to overcome the barrier of the GII.

The SPS process starts with an initial activation by applying a pulsed current while the powder is placed under pressure. The on–off DC current in this stage generates the spark discharge and rapid Joule heating between grains. Ionized elements from the particle's surface can be transformed into a plasma in some cases. The spark and plasma vaporize the contact area between particles, which cleans up the surface and draws together particles to create necks. The intensified Joule heating up to thousands of degrees Celsius and pressure make these necks develop and grow. The radiant Joule heating between particles also causes plastic deformation on the surface of the particles, which in turn enhances the consolidation. These features can enable completion of the material sintering in a very short period of time, even within 1 min in the case of the double perovskite presented in this work.

A direct reaction by firing the starting components of $CaCO_3$, MnO , and TiO_2 at ambient pressure gives rise to a mixture of perovskite $CaTiO_3$ and ilmenite $MnTiO_3$. $MnTiO_3$ will convert into Mn_2TiO_4 at higher temperatures. By changing the tilting group from $a^-a^-c^+$ of perovskite $CaTiO_3$ into the $a^+a^+c^-$, the insertion of Mn^{2+} at the A-site of $CaTiO_3$ can be achieved under high temperatures and a very modest pressure in a SPS synthesis, which also favors a columnar ordering of Ca and Mn columns along the c axis. The ilmenite $MnTiO_3$ and spinel Mn_2TiO_4 have lower melting temperatures than that of perovskite $CaTiO_3$. A prolonged sintering of $CaTiO_3 + MnTiO_3$ will result in a phase segregation between a solid phase and a liquid phase, which minimizes the Mn concentration in the perovskite. The pressure used in SPS is too small to influence the tolerance factor of the perovskite phase, but it helps to confine the oxides during the reaction. By

taking advantage of the nearly instant reaction with SPS, a significantly high concentration of Mn can enter into the A-site of the double perovskite without phase segregation; the maximum $x \approx 0.6$ in perovskite $Ca_{2-x}Mn_xTi_2O_6$ can be obtained at 100 MPa. Moreover, the graphite die used in SPS provides some reduction effect, which prevents Mn^{2+} from further oxidation during the reaction. The final manganese concentration in the product is determined by the measurement of magnetic susceptibility on the assumption of Mn^{2+} in the perovskite. The calculated valence based on the BVS from the structural data is also consistent with the amount of Mn^{2+} in the structure. As shown in the following paragraph, the manganese concentration in the samples made with SPS is sufficiently high to make the perovskite ferroelectric. The synthetic results are mapped out in the pressure–temperature phase diagram shown in the [Supporting Information](#).

One of the significant findings in this work is that the SPS sintering lowers the GII value of the double perovskite formula, so that a high pressure phase can be stabilized under a very modest pressure. Ionized elements from the particle's surface during SPS appear to change the dynamics of chemical reaction to form a bonding structure with a higher GII. This finding may make potentially the SPS method applicable to stabilize new metastable phases in a broader range of materials.

Crystal Structure through the Refinement of Neutron Powder Diffraction. Neutron powder diffraction experiments have been performed on $Ca_{2-x}Mn_xTi_2O_6$ ($x = 0.6$) in the temperature range of 1.5 to 700 K; patterns and the refinement results at selected temperatures are shown in [Figure 2](#). More

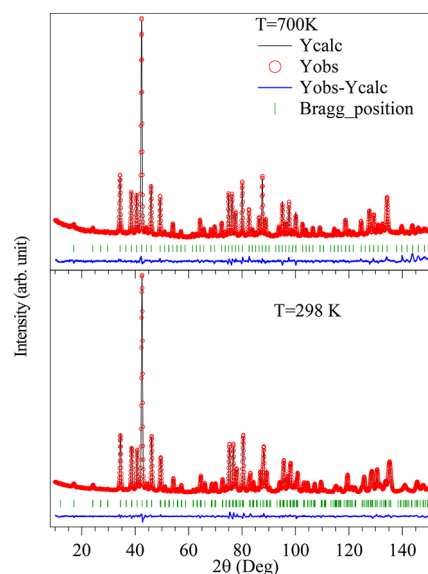


Figure 2. Neutron powder diffraction pattern and results of the refinement of $Ca_{1.4}Mn_{0.6}Ti_2O_6$. These patterns have been collected with the neutron beam ($\lambda = 1.59$ Å) at D2B, ILL, France.

detailed information about the refinement can be found in [Supporting Information](#). A structural transition at 570 K is marked by an anomaly in the temperature dependence of lattice parameters of [Figure 3\(a\)](#); a and c start to be separated at $T < 570$ K. The neutron diffraction pattern can be fit well by the structural models of nonpolar double perovskite $P4_2/nmc$ at $T > T_c$ and polar double perovskite $P4_1mc$ at $T < T_c$. These structural models have been used to fit XRD patterns of the double perovskite $CaMnTi_2O_6$ made under high pressure as

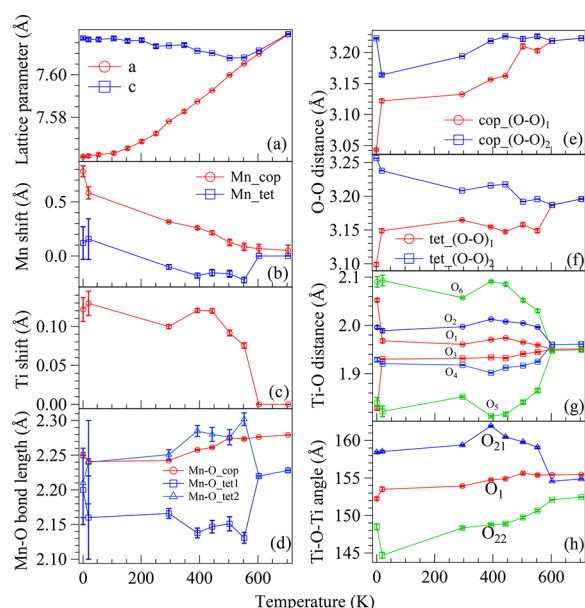


Figure 3. Temperature dependence of (a) lattice parameter, (b) the displacement for Mn at the tetrahedral site (tet) and the coplanar site (cop), (c) the displacement for Ti, (d) Mn–O bond lengths; (e) the nearest oxygen–oxygen distance at the coplanar site, (f) the nearest oxygen–oxygen distance at the tetrahedral site; (g) the Ti–O bond lengths at octahedral site; (h) Ti–O–Ti bond angles. Ferroelectric transition occurs at $T_c \sim 560$ K as determined by the SHG measurement, which is consistent with the result of structural study; clear structural transition occurs between sampling points of 550 and 600 K. The magnetic transition occurs at $T_N \sim 5$ K from the specific heat measurement. A superlattice peak due to diffraction from magnetic moments has been found in the neutron diffraction pattern collected at 1.5 K, and the pattern can be refined with the model of the polar structure plus type-C spin ordering at Mn sites.

illustrated in Figure 1. Although Ca apparently occupies partially the 2c site for Mn in addition to the 2a and 2b sites in the SPS product, the disorder does not destroy the columnar ordering of A-site cations in the double perovskite structure. The space group $P4_2/nmc$ allows Mn^{2+} on the coplanar site to move out of the square plane formed by four oxygen, but the moving direction remains random along the c axis in this nonpolar structure, which is why a finite displacement on the Mn site is obtained even at $T > T_c$, see Figure 3(b). The displacement shows no noticeable change on crossing the nonpolar to polar structural transition. However, right below T_c Mn on the tetrahedral-site is polarized in the opposite direction to that of the coplanar Mn; the polarization gradually changes sign as temperature decreases. Given nearly canceling electric dipoles from two Mn sites right below T_c , the net dipole moment comes from the TiO_6 array. A clear displacement of Ti occurs on cooling through T_c , as is shown in Figure 3(c). The Ti displacement in an octahedral-site with the $a^+a^-c^-$ tilting system is highly unusual and it must be induced by the A-site displacement. We will come back to this point in the following discussion.

The polar displacements of Mn and Ti ions create interesting changes of interatomic distances and bonding angles. While the changes of Mn–O bond length in the coplanar and in the tetrahedra sites of Figure 3(d) are consistent with the Mn displacement, the coplanar oxygen exhibit an unusual change from a square into a rectangle of Figure 3(e) on cooling through T_c . The MnO_4 tetrahedra also become distorted, i.e.,

they are elongated along the c axis, see Figure 3(f). The TiO_6 octahedra are no longer regular; the basal plane of an octahedron becomes rectangular below T_c . Since coplanar MnO_4 units share the apical oxygen and tetrahedron MnO_4 units share the oxygen in the basal plane of an octahedron, these local structural changes on cooling through T_c lead to corresponding changes in the Ti–O–Ti bonding angles of Figure 3(e); the bond angle increases along the a axis and decreases for the bonding along the direction 90° from the a axis in the basal plane. There is no change of the bond angle along the c axis. Calculations of BVS for each cation based on the structural data show that the Mn^{2+} at coplanar and tetrahedral sites have BVS values of 1.18 and 1.30, respectively, while the BVS value of the Ti^{4+} is 4.20, indicating that Mn–O is slightly under-bonded and Ti–O is slightly overbonded. We have further calculated the temperature dependence of GII for the whole structure. Presented in the Supporting Information, the GII increases slightly below T_c , which means that the ferroelectric transition further enlarges the degree of under-bonding and overbonding at different cation sites in the structure.

Physical Properties of the SPS Product. We have used the same SPS procedure to synthesize a series of perovskites $Ca_{2-x}Mn_xTi_2O_6$ ($0 < x \leq 0.6$). While XRD shows a single phase for all these compositions, it is difficult from the refinement alone to determine whether the phases are simple perovskite or have the polar double perovskite structure at room temperature, especially for compositions with the lower Mn concentration. We used the SHG microscopy to probe ferroelectricity, which is particularly useful in the cases where the structural distortion associated with a ferroelectric transition is too small to be detected by diffraction technique. Figure 4(a)

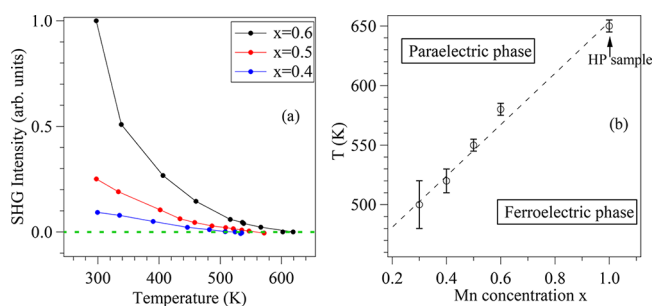


Figure 4. (a) Temperature dependence of the averaged SHG intensity for $Ca_{2-x}Mn_xTi_2O_6$ samples with different Mn concentrations. The polarized SHG detected by s-polarized incident beam. Green dashed line indicates the background noise level, which is close to zero. (b) The phase diagram of $Ca_{2-x}Mn_xTi_2O_6$. T_c of the SPS samples is defined from temperature-dependent measurements of SHG, where the SHG vanishes. The data for high-pressure sample are after ref 16.

shows the temperature dependence of the SHG of $Ca_{2-x}Mn_xTi_2O_6$ ($0.4 \leq x \leq 0.6$). When $x < 0.3$, SHG intensity is close to the background noise level because either Mn^{2+} is too diluted to form the polar double perovskite structure or the Curie temperature T_c is below room temperature. As shown in the phase diagram of Figure 4(b), T_c is linearly proportional to the composition x . All data points for the SPS samples and the high-pressure sample fall roughly on a straight line. This observation means that a solid solution $Ca_{2-x}Mn_xTi_2O_6$ with the double perovskite structure is formed by the SPS synthesis rather than a phase segregation into $CaTiO_3$ and $CaMnTi_2O_6$.

In comparison with the structural data of $\text{CaMnTi}_2\text{O}_6$ synthesized under high pressure, T_c appears to be related to the magnitude of the Mn displacement on the coplanar site in the nonpolar phase. We have also performed polarization measurements on the SPS samples, as presented in [Supporting Information](#). Due to the leaking problem caused by residual carbon in the SPS samples, the polarization curves look slightly different from typical ones³² by the conventional method. However, a normal polarization curve can be obtained by the PUND method.³³ The results indicate that the double perovskites $\text{Ca}_{2-x}\text{Mn}_x\text{Ti}_2\text{O}_6$ obtained by the SPS method are switchable ferroelectrics.

Magnetism and Ferroelectricity. Like the double perovskite $\text{CaMnTi}_2\text{O}_6$ synthesized under high pressure, the SPS samples exhibit a magnetic ordering at ~ 5 K as indicated by specific heat measurement. Neutron powder diffraction at low temperatures also detect reflections from the manganese sublattice. Due to the substitution of Ca on the Mn sites in the SPS samples, the intensity of magnetic-order-related reflections is rather weak and peaks look broader. The refinement converges only if the type-C antiferromagnetic model is used. The refinement, however, cannot distinguish the easy axis of magnetic moments at Mn sites. The higher order term of spin-orbit coupling for the Mn at the coplanar sites prefers a moment normal to the oxygen square plane. Our DFT calculations also show that the ground state with the type-C magnetic ordering has the lowest energy. More detailed information about the calculated results can be found in the [Supporting Information](#). The electron configuration t^3e^2 of the high-spin $\text{Mn}^{2+}:d^5$ is compatible with a weak antiferromagnetic $\text{Mn}^{2+}-\text{O}-\text{O}-\text{Mn}^{2+}$ superexchange interaction between Mn^{2+} columns; the superexchange spin-spin interaction between tetrahedral and coplanar Mn^{2+} along a column is antiferromagnetic and extremely weak. The overall ferromagnetic intracolumn coupling must be from magnetic dipole-dipole interactions. An important finding is that the Mn^{2+} displacement at the coplanar site of [Figure 3\(b\)](#) is further enhanced while the magnetic moment at the same site becomes ordered. This finding is opposite the conventional wisdom that magnetism and ferroelectric displacements do not coexist on the same site. Hill has argued that the superexchange interaction facilitating magnetism tends to optimize the local bonding structure so as to maximize the orbital overlap integral, which is always against the displacement required for ferroelectricity at octahedral sites.⁶ In the case of double perovskite $\text{Ca}_{2-x}\text{Mn}_x\text{Ti}_2\text{O}_6$, however, the intracolumn coupling is dominated by the magnetic dipole-dipole interaction, which appears to be compatible with the electric dipole associated with the Mn displacement at the coplanar site. The observation that the Mn displacement is enhanced in the AF state is consistent with the DFT calculations. By relaxing the Mn displacement, our calculations indicate that the Mn displacement increases by 0.009 Å in the type-C ordered phase relative to the nonmagnetic phase.

The Driving Force for the Ferroelectric Transition. For proper ferroelectricity, a double-well potential is formed due to a large gain of the orbital hybridization at the expense of elastic energy associated with the atomic displacements, which leads to a soft-mode transition to polar structures.³⁴ From the point of view of structural symmetry, a variety of octahedral-site tilting modes in the perovskite structure do not give rise to a polar structure since a rotation at one site is accompanied by an opposite rotation at adjacent sites, for example, in the $a^+a^+c^-$

tilting system of the double perovskite $\text{CaFeTi}_2\text{O}_6$. At $T > T_c$, $\text{Ca}_{2-x}\text{Mn}_x\text{Ti}_2\text{O}_6$ oxides share the same nonpolar double perovskite structure as that of $\text{CaFeTi}_2\text{O}_6$. However, there is a distinct difference between these two perovskites. Allowed by symmetry in the nonpolar $P4_2/nmc$ structure, Mn at coplanar sites in $\text{Ca}_{2-x}\text{Mn}_x\text{Ti}_2\text{O}_6$ moves out of the plane, but the direction of the movement is random between sites. In contrast, Fe at the same position in $\text{CaFeTi}_2\text{O}_6$ stays in the plane even though Mn^{2+} and Fe^{2+} cations have similar sizes. To understand why the coplanar Mn^{2+} move off the plane whereas the coplanar Fe^{2+} does not, a DFT calculation was done, which takes into account the second nearest neighbors of oxygen atoms. [Figure 5\(a\)](#) illustrates that the orbital occupation

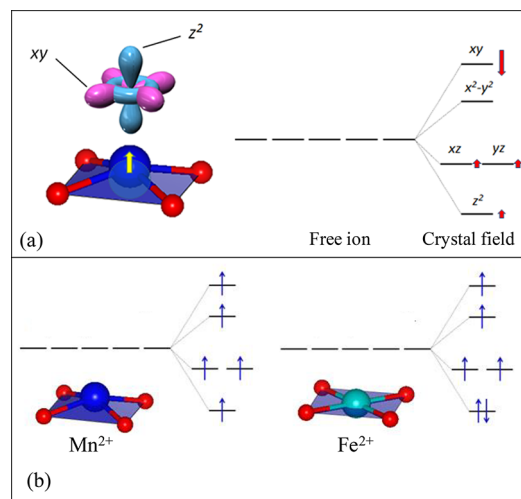


Figure 5. (a) Schematic drawing of the Mn displacement in a MnO_4 coplanar, xy and z^2 orbitals, and the orbital splitting for Mn^{2+} from a free ion to the site in the crystal field. Red arrows in the graph indicate the energy change as Mn^{2+} moves off the plane formed by four O^{2-} anions. The length of arrows is proportional to the magnitude of energy change associated with the Mn^{2+} displacement. (b) The orbital occupation of the coplanar site with Mn^{2+} and Fe^{2+} . Blue arrows represent spins. The double occupation of the z^2 orbital for Fe^{2+} offsets the energy reduction of xy orbital associated with the Mn^{2+} displacement, so that Fe^{2+} remains in the plane as observed. This drawing is based on DFT calculation presented in [Supporting Information](#).

number of d electrons is a key to the displacement of the Mn^{2+} . The coplanar symmetry stabilizes the z^2 orbital and destabilizes the antibonding xy orbital. Moving the cation out of the plane lowers the xy -orbital energy, but it increases the energies of the z^2 and $yz \pm izx$ orbitals; the net energy change still favors a Mn^{2+} ion moving out of the plane, as can be seen from the total energy change for Mn^{2+} at the center versus off-center provided in the [Supporting Information](#). In contrast, the occupation of the z^2 orbital by an extra electron in Fe^{2+} ion costs more energy for the displaced Fe^{2+} relative to that within the plane, as illustrated in [Figure 5\(b\)](#). While the consideration of the orbital occupation can justify the displacement of Mn^{2+} , it is not directly related to the transition to a polar structure.

The $a^+a^+c^-$ tilting system of the $P4_2/nmc$ structure creates the MnO_4 square planes that share the apical oxygen of the adjacent four TiO_6 octahedra. The tilting system changes from the $a^+a^+c^-$ to the $a^+b^+c^-$ at the phase transition to the polar $P4_2mc$ structure as reflected in the temperature dependence of the Ti—O—Ti bond angles in [Figure 3\(h\)](#) on cooling through

T_c . As a result, the coplanar MnO_4 changes from a square in the nonpolar phase to a rectangle in the polar phase. The longer edge of the rectangle causes a reduction of the octahedral-site tilting around the axis normal to the longer edge of the rectangle. At $T > T_c$, since the Mn displacement is random at coplanar sites, the local tilting pattern must be a mixture of the $a^+b^+c^-$ and $b^+a^+c^-$. It is impossible to detect the local tilting system by diffraction technique, so that the $a^+a^+c^-$ is used as the global tilting system in the refinement of diffraction pattern at $T > T_c$. Since TiO_6 octahedra share corners to form a 3D network in the perovskite structure, a mixture of the $a^+b^+c^-$ and $b^+a^+c^-$ in the local tilting system would create significant bond length mismatch and stresses and raise the system elastic energy as illustrated in Figure 6. One obvious change from the nonpolar

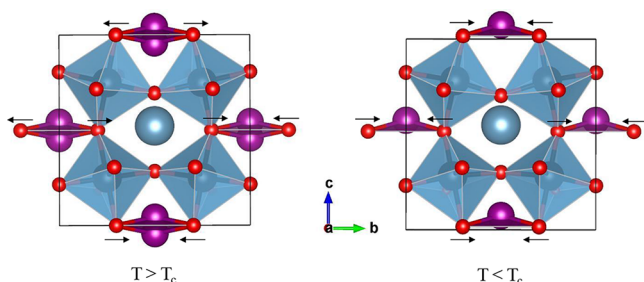


Figure 6. Structural models projected along the a axis. Only the Mn at coplanar sites and Ti at octahedral site are shown in the drawing. Arrows point to the direction of oxygen displacement associated with the rotation of O_4 plane. For the oxygen moves toward the Mn, the longer axis of the O_4 rectangle is parallel to the a axis. It is along the b axis for oxygen moves away from the Mn. The cooperative octahedral-site rotation requires a uniform reduction of the O–O distance at coplanar sites. The disorder of the Mn displacement direction and associated rectangle orientation at $T > T_c$ destroys the cooperativity of the octahedral-site rotation and increases the elastic energy of the structure. The tendency to lower the elastic energy is the driving force for ordering the displacement direction at Mn sites and therefore the ferroelectric transition.

to the polar structural transition is to increase the cooperativity of the octahedral-site tilting in the structure, which lowers the system energy. Starting with the nonpolar structure having the coplanar Mn in up-and-down positions and allowing the lattice to be relaxed, our DFT calculation always gives a ground state having ordered Mn displacement at the coplanar sites. The thermodynamics of this order–disorder transition should be described with the Landau theory by using a ratio of ordered Mn versus the total number of coplanar Mn as the order parameter. In reality, the displacement of Ti serves better as an order parameter.

The double perovskite $\text{Ca}_{2-x}\text{Mn}_x\text{Ti}_2\text{O}_6$ represents a new type of ferroelectricity. While a polar structure is generally prohibited in all tilting systems of the perovskite structure, the polar mode in the Ti–O array is induced by the lattice distortions associated with the order–disorder transition at the coplanar Mn sites, which is similar to the improper ferroelectric YMnO_3 . For proper ferroelectricity, a depolarization field will suppress the dipole formation as the sample thickness becomes small, viz the so-called critical thickness problem, which is a major hurdle for applying this type of ferroelectric material.³⁵ Although a screening technique has been applied to minimize the depolarization field, it is difficult to completely suppress the depolarization field. Whether the order–disorder type ferroelectric is superior to a proper ferroelectric in terms of the

resistance to the depolarization field remains to be explored experimentally. Moreover, our DFT calculations indicate that a similar order–disorder type of ferroelectricity can be realized in other double perovskite CaMnM_2O_6 ($M = \text{Zr}^{4+}$, Sn^{4+} and Ge^{4+}). $\text{CaMnGe}_2\text{O}_6$ would have a larger displacement of Mn at the coplanar site, the smallest octahedral-site tilting, and the highest dipole moment. In addition, a simulation with a 1.5% compressive strain on the ferroelectric $\text{CaMnTi}_2\text{O}_6$ leads to about 16.5% enhancement of the net dipole moment.

4. CONCLUSION

In summary, we have developed a new procedure to synthesize gram-level new ferroelectric $\text{Ca}_{2-x}\text{Mn}_x\text{Ti}_2\text{O}_6$. By using neutron powder diffraction and first-principles calculations, we have identified the origin causing the ferroelectric transition. Unlike proper ferroelectricity where dipoles are generated directly from the displacement associated with softening of a polar mode in the high symmetry paraelectric phase, the order–disorder transition at the coplanar Mn^{2+} site leads to a polar structure in which dipoles are created at Ti^{4+} sites, the Mn^{2+} tetrahedral sites, and Mn^{2+} at the coplanar sites. The Curie temperature for the ferroelectric transition is about 560 K and this new type of ferroelectricity has the potential to overcome the critical thickness problem experienced in the proper ferroelectric materials for practical applications. The new mechanism of ferroelectricity and the method for the material synthesis presented in this work provide an exciting new direction to the search for new ferroelectric materials.

■ ASSOCIATED CONTENT

Supporting Information

The Supporting Information is available free of charge on the ACS Publications website at DOI: 10.1021/jacs.7b11219.

Further structural refinement results, electronic calculation results, the results of polarization measurement, and the pressure–temperature phase diagram of $\text{Ca}_{1.4}\text{Mn}_{0.6}\text{Ti}_2\text{O}_6$ (PDF)

■ AUTHOR INFORMATION

Corresponding Author

*jszhou@mail.utexas.edu

ORCID

Jose A. Alonso: 0000-0001-5329-1225

Graeme Henkelman: 0000-0002-0336-7153

John B. Goodenough: 0000-0001-9350-3034

Jianshi Zhou: 0000-0002-7667-5640

Notes

The authors declare no competing financial interest.

■ ACKNOWLEDGMENTS

This work was supported by Gordon and Betty Moore Foundation EPIQS Initiative through a sub-contract to Grant No. GBMF4534 and was partially supported by the National Science Foundation through the Center for Dynamics and Control of Materials: an NSF MRSEC under Cooperative Agreement No. DMR-1720595 in USA and JSPS KAKENHI Grant number 26410078, 15H04128, and JP16H6439, and MEXT-Supported Program for the Strategic Research Foundation at Private Universities, 2015–2019 in Japan. JBG, GH, and MCD were supported by Welch Foundation, Houston, Texas, in USA with grant number F-1066, F-1841,

and F-1038. JAA and MTFD acknowledge the Spanish MINECO for funding the project MAT2013-41099-R. JQY is supported by the U.S. Department of Energy, Office of Science, Basic Energy Sciences, Materials Sciences and Engineering Division. The neutron diffraction work at ORNL's Spallation Neutron Source was sponsored by the Scientific User Facilities Division, Office of Basic Energy Sciences, U.S. Department of Energy.

REFERENCES

- (1) Goodenough, J. B.; Longo, J. M. In *Numerical Data and Functional Relationships in Science and Technology*; Hellwege, K.-H., Ed.; Landolt-Bornstein: Berlin, 1970; Vol. 4a, p 126.
- (2) Xu, Y. H. *Ferroelectric Materials and Their Applications*; North Holland: Amsterdam, 1991.
- (3) Takesada, M.; Itoh, M.; Yagi, T. *Phys. Rev. Lett.* **2006**, *96*, 227602.
- (4) Hidaka, T. *Ferroelectrics* **2003**, *283*, 11.
- (5) Yamada, Y.; Todoroki, N.; Miyashita, S. *Phys. Rev. B: Condens. Matter Mater. Phys.* **2004**, *69*, 024103.
- (6) Hill, N. A. *J. Phys. Chem. B* **2000**, *104*, 6694.
- (7) Benedek, N. A.; Fennie, C. J. *J. Phys. Chem. C* **2013**, *117*, 13339.
- (8) Takahashi, R.; Ohkubo, I.; Yamauchi, K.; Kitamura, M.; Sakurai, Y.; Oshima, M.; Oguchi, T.; Cho, Y.; Lippmaa, M. *Phys. Rev. B: Condens. Matter Mater. Phys.* **2015**, *91*, 134107.
- (9) Kim, T.; Puggioni, D.; Yuan, Y.; Xie, L.; Zhou, H.; Campbell, N.; Ryan, P.; Choi, Y.; Kim, J.-W.; Patzner, J. *Nature* **2016**, *533*, 68.
- (10) Knapp, M. C.; Woodward, P. M. *J. Solid State Chem.* **2006**, *179*, 1076.
- (11) King, G.; Woodward, P. M. *J. Mater. Chem.* **2010**, *20*, 5785.
- (12) Shimakawa, Y. *Inorg. Chem.* **2008**, *47*, 8562.
- (13) King, G.; Thimmaiah, S.; Dwivedi, A.; Woodward, P. M. *Chem. Mater.* **2007**, *19*, 6451.
- (14) Fukushima, T.; Stroppa, A.; Picozzi, S.; Perez-Mato, J. M. *Phys. Chem. Chem. Phys.* **2011**, *13*, 12186.
- (15) King, G. Ph.D. thesis, The Ohio State University, Columbus, OH, 2009.
- (16) Aimi, A.; Mori, D.; Hiraki, K.-i.; Takahashi, T.; Shan, Y. J.; Shirako, Y.; Zhou, J.; Inaguma, Y. *Chem. Mater.* **2014**, *26*, 2601.
- (17) Leinenweber, K.; Parise, J. J. *Solid State Chem.* **1995**, *114*, 277.
- (18) Benedek, N. A.; Fennie, C. J. *Phys. Rev. Lett.* **2011**, *106*, 107204.
- (19) Rodriguez-Carvajal. *Phys. B* **1993**, *192*, 55.
- (20) Blöchl, P. E. *Phys. Rev. B: Condens. Matter Mater. Phys.* **1994**, *50*, 17953.
- (21) Kresse, G.; Joubert, D. *Phys. Rev. B: Condens. Matter Mater. Phys.* **1999**, *59*, 1758.
- (22) Kresse, G.; Furthmüller, J. *Phys. Rev. B: Condens. Matter Mater. Phys.* **1996**, *54*, 11169.
- (23) Kresse, G.; Hafner, J. *Phys. Rev. B: Condens. Matter Mater. Phys.* **1993**, *47*, 558.
- (24) Kresse, G.; Hafner, J. *Phys. Rev. B: Condens. Matter Mater. Phys.* **1994**, *49*, 14251.
- (25) Byeon, S. H.; Lee, S. S.; Parise, J. B.; Woodward, P. M.; Hur, N. H. *Chem. Mater.* **2005**, *17*, 3552.
- (26) Byeon, S. H.; Lee, S. S.; Parise, J. B.; Woodward, P. M. *Chem. Mater.* **2006**, *18*, 3873.
- (27) Byeon, S. H.; Lufaso, M. W.; Parise, J. B.; Woodward, P. M.; Hansen, T. *Chem. Mater.* **2003**, *15*, 3798.
- (28) Byeon, S. H.; Lee, S. S.; Parise, J. B.; Woodward, P. M.; Hur, N. H. *Chem. Mater.* **2004**, *16*, 3697.
- (29) Chen, W.; Mizumaki, M.; Saito, T.; Shimakawa, Y. *Dalton Trans.* **2013**, *42*, 10116.
- (30) Lufaso, M. W. Ph.D. thesis, The Ohio State University, Columbus, OH, 2002.
- (31) Larregola, S. A.; Zhou, J. S.; Alonso, J. A.; Pomjakushin, V.; Goodenough, J. B. *Inorg. Chem.* **2014**, *53*, 4281.
- (32) Rabe, K. M.; Ahn, C. H.; Triscone, J.-M. *Physics of Ferroelectrics: A Modern Perspective*; Springer-Verlag: Berlin, 2007; Vol. 105.
- (33) Fukunaga, M.; Noda, Y. *J. Phys. Soc. Jpn.* **2008**, *77*, 064706.
- (34) Cohen, R. E. *Nature* **1992**, *358*, 136.
- (35) Benedek, N. A.; Stengel, M. *Physics* **2014**, *7*, 32.
- (36) Belik, A. *Dalton Trans.*, accepted manuscript, DOI: [10.1039/C7DT04490A](https://doi.org/10.1039/C7DT04490A).
- (37) Gou, G.; Charles, N.; Shi, J.; Rondinelli, J. M. *Inorg. Chem.* **2017**, *56*, 11854.

NOTE ADDED IN PROOF

After the manuscript was accepted for publication, we became aware of two relevant works published recently. Belik³⁶ has given a comprehensive review about the A-site columnar-ordered $A_2A''B_4O_{12}$. The review includes all possible cations which can occupy the tetrahedral site or the coplanar site or both sites. It is a useful guide for designing new multiferroic materials with the framework of quadruple perovskites. In another paper, Gou et al.³⁷ have predicted the ferroelectric-photovoltaic property of the double perovskite $\text{CaMnTi}_2\text{O}_6$ based on a DFT calculation. They have also found that the C-AFM state has the lowest energy, which is consistent with our results from the refinement of neutron diffraction and DFT calculations.